



HAL
open science

Support Effects Examined by a Comparative Theoretical Study of Au, Cu and CuAu Nanoclusters on Rutile and Anatase Surfaces

Marwa Dhifallah, Mathilde Iachella, Adnene Dhouib, Francesco Di Renzo,
David Loffreda, Hazar Guesmi

► **To cite this version:**

Marwa Dhifallah, Mathilde Iachella, Adnene Dhouib, Francesco Di Renzo, David Loffreda, et al.. Support Effects Examined by a Comparative Theoretical Study of Au, Cu and CuAu Nanoclusters on Rutile and Anatase Surfaces. *Journal of Physical Chemistry C*, 2019, 123 (8), pp.4892-4902. 10.1021/acs.jpcc.8b11812 . hal-02019069

HAL Id: hal-02019069

<https://hal.science/hal-02019069>

Submitted on 1 Dec 2020

HAL is a multi-disciplinary open access archive for the deposit and dissemination of scientific research documents, whether they are published or not. The documents may come from teaching and research institutions in France or abroad, or from public or private research centers.

L'archive ouverte pluridisciplinaire **HAL**, est destinée au dépôt et à la diffusion de documents scientifiques de niveau recherche, publiés ou non, émanant des établissements d'enseignement et de recherche français ou étrangers, des laboratoires publics ou privés.

Support Effects Examined by a Comparative Theoretical Study of Au, Cu and CuAu Nanoclusters on Rutile and Anatase Surfaces

Marwa DHIFALLAH^{1,2}, Mathilde IACHELLA³, Adnène DHOUIB⁴, Francesco DI RENZO¹, David LOFFREDA^{3*} and Hazar GUESMI^{1*}

¹*Institut Charles Gerhardt Montpellier, UM/CNRS/ENSCM, 240, Avenue du Professeur Emile Jeanbrau, 34090 Montpellier, France.*

²*Université de Gabes, Unité de recherche environnement, Catalyse et Analyse des Procédés, 6072 Gabes, Tunisie.*

³*Univ Lyon, Ens de Lyon, CNRS UMR 5182, Université Claude Bernard Lyon 1, Laboratoire de Chimie, F-69342, Lyon, France.*

⁴*College of Sciences, Department of Chemistry, Imam Abdulrahman Bin Faisal University, 31113 Dammam City, Saudi Arabia.*

Corresponding authors: david.loffreda@ens-lyon.fr; hazar.guesmi@enscm.fr

Abstract

The role of the support anatase TiO₂(100) and rutile TiO₂(110) on the energetics, the shape and the charge transfer of deposited CuAu nanoclusters (~ 1 nm) has been examined by using density functional theory calculations including Hubbard correction (DFT+U). Regular

truncated octahedron clusters (rto), $\text{Cu}_{(1-x)}\text{Au}_{(x)}$ (x being in the range 0.15-0.36), representing different alloy types (core@shell, Regular alloy, Skin-Heart) are considered. From a thermodynamic standpoint, the core-shell deposited nanoclusters present the strongest adsorption strength on both rutile and anatase supports, although they are the least stable homotops in vacuum. Interestingly, for skin-heart and regular alloy CuAu clusters, the stability on these supports decreases with the Au content. CuAu nanoclusters present larger adsorption energies on rutile than on anatase support. This result has been explained by a Bader analysis of charge transfers and an energy decomposition analysis (EDA) model which shows a larger binding energy between the metal and the rutile support than that on anatase, in part compensated by the stronger deformation of the structure of rutile. At the size of 38 atoms, the bimetallic cluster exhibits a significant propensity to distort its structure and adapt it to the geometry of the oxide surface to maximize the stability of the formed metal-oxide chemical bonds. Such an interesting property is expected to decay with the increasing size of the metallic nanocluster. This work provides an original discussion related to the support effect which is rarely evoked in the literature of DFT studies of such supported alloy clusters at the nanoscale.

I-Introduction

Supported bimetallic nanoparticles (BiM NPs) are widely used as heterogeneous catalysts [1-4]. In the recent decade, these materials have attracted much attention due to their tunable catalytic properties. In fact, for several catalyzed reactions, alloying two metals could improve the activity and/or the selectivity compared to the properties measured for the same reactions occurring on monometallic components [5-6]. The catalytic properties of the supported metals may depend on several factors, such as the size and the shape of the nanoparticles, the structure and the surface composition, the stability of the nanoparticles and their interactions with the support. Although these factors have been identified for a long time, a rational control and understanding of the catalytic properties at the atomic scale is still missing.

Many methods have been employed for the synthesis and the characterization of BiM NPs on various oxide supports [7]. Supported Au-based NPs, such as AuPd [8-9], AuCu [10-12], AuAg [13-14], and AuPt [15-16] are highly active for many catalytic reactions, such as CO oxidation, and can be applied in catalysis, electrochemistry and nanotechnology [17-18]. The AuCu/TiO₂ system has been employed several times for various applications such as wastewater treatment [19], photocatalysis and CO₂ reduction by water [20] and photodegradation of methyl orange [21].

Titanium dioxide is one of the most widely used and studied reducible supports in the literature [22]. TiO₂ supports for heterogeneous catalysts provide stability in electrochemical environment and are easily commercially available [23-24]. Different allotropic forms of TiO₂ exist in the nature: anatase, rutile and brookite. Among them, anatase and rutile feature the most interesting surfaces for applications on photochemistry [25,26] and photocatalysis, especially for the Au/TiO₂ system [24,27-29]. The role of the support is often considered in the literature and a classification has been proposed for catalysis by gold according to two major effects : reducibility and strong-metal support interactions [30]. Nevertheless, the role

of the support on the chemical properties of those BiM NPs is still debatable [31]. The nature and the structure of the surface active sites is still the subject of intense research and discussions [32-33].

During the last decade, several theoretical works have reported on the growth of Au clusters (between 4 and 10 atoms) on titanium support [34-39]. Larger Au clusters (20-24 atoms) in interaction with the rutile stoichiometric $\text{TiO}_2(110)$ surface have been modeled by combining DFT calculations with a genetic algorithm [40-42]. The AuCu bimetallic system has been studied several times from global optimization methods, with free clusters containing 38-56 atoms [43-48]. Complex morphologies and shapes have been found including (poly)icosahedral forms [44-45], distorted and pancake shapes [45], and a wide and complex range of structures including core-shell systems [47-48]. However, the deposit of AuCu on the titania support, has been studied by density functional theory calculations only by considering small clusters of 3 atoms [49] or solid-solid AuCu(001)/ $\text{TiO}_2(101)$ interfaces [50]. Hence, little is known about the interaction of gold-copper BiM NPs at a larger size (around 1 nm) on the titanium support and the quantitative description of the effect of the different forms (anatase *vs.* rutile) is still missing.

In order to fill this gap, this work aims to compare the effect of the surface of anatase and rutile supports on the shape and the stability of either monometallic gold and copper nanoparticles or gold-copper nanoalloys for 38 atoms in total (around 1 nm). The paper is organized as follows: first, the optimized parameters of both TiO_2 supports are reported. Then the results of the optimizations of free nanoclusters are analyzed. In the third part, thermodynamic and geometric data of deposited Au, Cu, CuAu nanoclusters are exposed by comparison between rutile and anatase. Electronic structure calculations with the Bader charge analysis are discussed.

II-Computational details

Periodic DFT calculations were performed using the projector-augmented wave (PAW) method [51-52], as implemented in the Vienna *ab initio* simulation package (VASP) code [53]. The generalized-gradient approximation functional of the exchange–correlation energy was calculated within the Perdew, Burke, and Ernzerhof formulation (GGA-PBE) [54]. The cut-off energy was fixed at 400 eV and the positions of the atoms in the supercell are relaxed until the total electronic energy differences fall below 10^{-6} eV.

DFT calculations of rutile and anatase oxide supports faces a classical issue of band-gap underestimation [55], with a width of 1.7 eV for rutile with GGA-PBE vs 3.05 eV experimentally and a width of 2.1 eV for anatase with GGA-PBE vs 3.2 eV experimentally [56]. Indeed, both LDA and GGA functionals fail to describe the corresponding electron localization at a metallic center [57]. This is explained by the narrow radial extension of Ti $3d$ orbitals. In titanium oxide, the $3d$ orbitals do not overlap with the oxygen ones and they are more localized on the titanium atoms. A probative semi empirical approach has been proposed to improve the spurious delocalization provided by LDA and usual GGA functionals. An additional term U , corresponding to electron on-site repulsion and based on a Hubbard model [58-59], is considered to correct the self-interaction error. In this work, the Dudarev’s approach (PBE+ U) has been selected [60] with an optimal value for the Coulomb interactions corrections of Ti electrons U_{eff} of 4.2 eV for rutile and of 3.3 eV for anatase. The systematic error of the band gap has been evaluated by changing the extension of the Ti atom valence (see for instance, M. Iachella et al. [61] for more details). In this study, we have chosen to describe the Ti^{4+} states by selecting 12 valence electrons for Ti atoms ($3s^2 3p^6 3d^2 4s^2$).

TiO_2 rutile and anatase bulks were modeled using tetragonal unit cells with $a = b \neq c$ and $\alpha = \beta = \gamma = 90^\circ$. For the DFT calculations, Monkhorst-Pack [62] k-points mesh of $(9 \times 9 \times 15)$ and

($33 \times 33 \times 13$) have been considered, respectively, for rutile and anatase. Extended surfaces (see Figure 1) were modeled by bi-dimensional periodic slabs with the vacuum space between two equivalent slabs along the z direction set to 20 Å. The rutile TiO₂(110) surface has been described by a stoichiometric non-polar termination within a (6 × 3) supercell terminated by bridging oxygen rows along y (Figure 1a). As the number of atoms in a trilayer TiO₂ rutile is large (36 Ti and 72 O atoms), we considered a TiO₂ slab with only 3 trilayers (representing 324 atoms in total). In this model the bottommost layer was fixed in bulk optimal positions and the two topmost layers were allowed to fully relax. The anatase TiO₂(100) surface was described by a (5 × 2) supercell composed of 240 atoms distributed over 4 layers with the two bottommost layers fixed to the bulk situation (Figure 1b). Converged total electronic energies of bare surfaces were calculated by choosing k-points grids (smallest supercells) ($7 \times 7 \times 1$) and ($3 \times 3 \times 1$) for rutile TiO₂(110) and anatase TiO₂(100), respectively. For deposited metallic nanoclusters, larger supercells have been considered so the gamma-point only approach was used.

Insert Figure 1

The surface energies γ (meV.Å⁻²) of the two TiO₂ supports are calculated as the difference between the total energy of the slab and the total energy of an equal number of TiO₂ units in the bulk phase, divided by the total exposed area.

Spin polarized calculations were developed for free monometallic Au, Cu, and bimetallic CuAu nanoparticles (BiM NPs). During the geometric optimizations, all the degrees of freedom of the metallic atoms were relaxed. In order to avoid spurious interactions between cluster images, the considered supercells were large (30x30x30 Å³). The Brillouin zones were sampled by gamma point with a convergence criterion for total electronic energy set to 10⁻⁶ eV. Atomic positions and lattice parameters were both relaxed until residual forces are below 0.01 eV Å⁻¹. In this work we focused on the Cu-rich phase of Cu_{1-x}Au_x nanoalloys, in which

the composition on Au increased from $x=0.15$ to $x=0.36$. According to previous works related to the theoretical study of gold-copper nanoclusters in vacuum [see 43 and references therein], there exist several possible morphologies in the fluxional regime around 1 nm [44-48], including octahedral, decahedral and icosahedral shapes. Due to the computational cost, the exploration of all possible shapes on TiO₂ support is not possible in a reasonable time. To open the discussion of the support effect on the nanocluster stability and structure, we have chosen to represent monometallic Au and Cu and bimetallic CuAu systems by regular truncated octahedral (rto) nanoparticles of 38 atoms based on the fcc packing of the corresponding bulk crystals. Five CuAu structures representing three different nanoalloy types (core-shell (CS), skin-heart (SH) and regular alloy (RA)) were computed. Of course this Au-Cu structure selection is not inclusive. In addition to the selected structures, there are a plenty of Au-Cu structures that could exist. However, all structures can't be taken into account by conventional DFT calculations. In this work, the rto(38) structure give the possibility to compare a "perfect" core-shell structure (6 atoms in the core and 32 atoms in the shell) with different alloyed structures, but many other possibilities could exist. In order to analyze the stability of these different chemical ordering structures of CuAu as a function of the Au content x , the excess energy per atom (ΔE_{exc}) was calculated [63-65]. This energetic descriptor is defined as follows:

$$\Delta E_{exc}(Cu_mAu_n) = E(Cu_mAu_n) - \frac{mE(Cu_{38})}{N} - \frac{nE(Au_{38})}{N} \quad \text{Eq.1}$$

where $E(Cu_mAu_n)$ is the total electronic energy of the BiM NP and $E(Cu_{38})$ and $E(Au_{38})$ are respectively the total electronic energies of the structures of the pure 38 rto NPs. By this way, E_{exc} is unbiased, being zero for pure clusters. A negative value of excess energy indicates a tendency to form stable nanoalloys (the mixing is energetically favorable), and the lower the value of excess energy, the higher the stability of the structure is. In addition, the surface energies of these free NPs are calculated as follows:

$$\gamma(x) = \frac{E_{tot}(x) - \overline{E_{tot}}(x)}{A} \quad \text{Eq.2}$$

where $E_{tot}(x)$ is the total electronic energy (calculated by DFT) of the optimized structure of the bimetallic nanoparticle of composition x , $\overline{E_{tot}}(x)$ is the total electronic energy of the optimal alloy bulk with an equivalent composition x , and A is the surface area of the corresponding relaxed nanoparticles structure. More details concerning the surface energy calculations could be found elsewhere [66].

In order to evaluate the effect of the interaction of the nanoclusters with the oxide support, different energetic descriptors were computed. The first one corresponds to the energy gained $\Delta E_{deposition}^{NP/TiO_2}$ by the system after the deposition of the gas phase NP on the TiO_2 oxide support and calculated as follows:

$$\Delta E_{deposition}^{NP/TiO_2} = E(NP/TiO_2) - E(TiO_2) - E(NP_{free}) \quad \text{Eq.3}$$

where $E(NP/TiO_2)$ is the total electronic energy of the deposited NP on the support, $E(TiO_2)$ represents the total electronic energy of the bare TiO_2 support (anatase and rutile surfaces with spin-polarization) and $E(NP_{free})$ is the energy of the 38 rto NP calculated in gas phase. The second energetic descriptor corresponds to the average deposition energy $\langle \Delta E_{deposition}^{NP/TiO_2} \rangle$ per bond connecting the NP to the support. This value is obviously based on the first descriptor, which has been normalized by the number of bonds between the NP and the TiO_2 ($N_b^{NP-TiO_2}$):

$$\langle \Delta E_{deposition}^{NP/TiO_2} \rangle = \frac{E(NP/TiO_2) - E(TiO_2) - E(NP_{free})}{N_b^{NP-TiO_2}} \quad \text{Eq.4}$$

As described in Refs. [67-68], the deposition energy $\Delta E_{deposition}^{NP/TiO_2}$ can be decomposed in two energetic components: the deformation energy and the interaction energy. It is also interesting to quantify the deformation energy of the NP before and after the deposition on the support, named ΔE_{deform}^{NP} and defined as follows:

$$\Delta E_{deform}^{NP} = E(NP^*) - E(NP_{free}), \quad \text{Eq.5}$$

where $E(NP^*)$ is the total electronic energy of the NP relaxed on TiO₂ support, obtained by a single point energy calculation in vacuum.

In addition to these components, it is also important to evaluate the deformation energy of the stoichiometric TiO₂ support during the deposition $\Delta E_{deform}^{TiO_2}$

$$\Delta E_{deform}^{TiO_2} = E(TiO_2^*) - E(TiO_2) \quad \text{Eq.6}$$

Where $E(TiO_2^*)$ and $E(TiO_2)$ are respectively the total electronic energies of the bare support after and before deposition. TiO_2^* is the bare support relaxed after the NP deposition, for which we have performed a single point energy calculation.

The last component is the interaction energy (or binding energy) between the NP and the support, obtained when the deformation and the relaxation contributions are taken off from the deposition energies, as follows:

$$\Delta E_{interaction}^{NP^*/TiO_2^*} = \Delta E_{deposition}^{NP/TiO_2} - (\Delta E_{deform}^{NP} + \Delta E_{deform}^{TiO_2}) \quad \text{Eq.7}$$

Similarly to the case of the deposition energy, it is possible to normalize the interaction energy between the NP and the support per bond:

$$\langle \Delta E_{interaction}^{NP^*/TiO_2^*} \rangle = \frac{\Delta E_{deposition}^{NP/TiO_2} + \Delta E_{deform}^{NP} + \Delta E_{deform}^{TiO_2}}{N_b^{NP-TiO_2}} \quad \text{Eq.8}$$

In order to quantify the geometric deformation of the NP induced by the support, we have evaluated the geometric deformation ratio r_{deform} by calculating the average metal-metal bond length inside the NP before and after the deposition on the support. Then, we have applied the following formula:

$$r_{deform} = \left(\frac{\overline{d_{M-M}^{NP^*}}}{\overline{d_{M-M}^{NP}}} - 1 \right) \times 100 \quad \text{Eq.8}$$

Where $\overline{d_{M-M}^{NP^*}}$ is the average distance of M-M bonds of the deformed NP on the support and $\overline{d_{M-M}^{NP}}$ the average metal-metal bond length of the NP optimized in gas phase.

Finally, the electronic structure of modeled systems was studied through a charge transfer analysis based on Bader charge [69]. These calculations have been performed by using Henkelman and co-workers' approach interfaced with VASP [70].

III-Results

III.1. Modeling of TiO₂ supports

Extended surfaces are modeled by considering bi-dimensional periodic slab, involving a finite number of atomic layers, cut from the optimized bulk materials. All geometric and energetic parameters of optimized bulk rutile and anatase are depicted in table 1S. One important characteristic of the surface models is the choice of termination and thickness of the symmetric slab on the basis of the convergence of the surface energy (systematic error due to the slab thickness). In addition, as the focus herein is on the effect of the support, it is useful to give a brief description of the atomic structure of these two surfaces.

Rutile TiO₂(110) : the [110] direction in rutile TiO₂ leads to three types of terminations, where only one presents a stoichiometric surface (the one considered herein). It exhibits two-fold coordinated oxygen atoms (O_{2C}) rows upon the surface and Ti_{5C}/O_{3C} plan. Following the (110) direction, one can distinguish a Ti₂O₄ layer that is composed of three plans: two plans containing one oxygen and a third one in between composed of Ti₂O₂ (see Figure 1a). The relaxation of a stoichiometric rutile TiO₂ (110) surface has been estimated by ion-scattering spectroscopy. It appears that the height of O_{2C} from the surface is not different from the O-(TiO) distance in the bulk structure. A detailed analysis of surface energy (E_{surf}) calculations for stoichiometric surface model as a function of the slab thickness shows that absolute convergence is obtained for a 13-layer thick slab (0.362 J.m⁻² with a systematic error of ±10 mJ.m⁻²). This value is in fair agreement with previous DFT models (0.35 J.m⁻² [73]). Because of the computational cost, a reasonable compromise to make the theoretical study possible is to consider 3-layer thick slab, which leads to a larger systematic error of around 70 mJ.m⁻².

Anatase TiO₂(100): the (100) termination is very common in titanium oxide powder used in catalysis but the (101) facet was the most studied as it was reported to be the most thermodynamically stable TiO₂ anatase facet. Indeed, the calculated average surface energies was reported to follow the order of: $\gamma(110) 1.09 \text{ J m}^{-2} > \gamma(001) 0.9 \text{ J m}^{-2} > \gamma(100) 0.53 \text{ J m}^{-2} > \gamma(101) 0.44 \text{ J m}^{-2}$ [73]. Recent first-principles calculations reported by Ma et al. predict the relative photooxidation ((100) > (101) > (001)) and photoreduction ((100) > (101) > (001)) activities, and show the higher photocatalytic activity of (100) facet compared to the (101) and (001) surfaces [74]. Thus, because of its recently identified high reactivity and as very little is known about it, the TiO₂ (100) anatase surface was selected in this study. The outermost layer involves five coordinated (Ti_{5C}), two-fold (O_{2C}) and three-fold (O_{3C}) atoms, while the second layer exposes fully coordinated Ti and O atoms. It possesses small grooves formed by oxygen atoms (O_{2C}) on either side of the groove along with both Ti and O atoms at the bottom. From the analysis of surface energy evolution as a function of the slab thickness, an accurate convergence could be reached for 6-layer thick slab (12 atomic plans) with surface energy of 0.67 J.m⁻². This value is slightly higher than the value reported by Lazzeri et al 0.58 J.m⁻² [73]). To reduce the computational cost, a slab with a thickness of 2 layers was considered, which leads to a larger systematic error of 10 mJ.m⁻².

III.2. Gas phase NPs

In a recent DFT work devoted to the study of the stability of bimetallic AuCu NPs in vacuum, Iachella and coworkers [66] have established a stability-composition relation for a set of two hundreds of BiM NP, in the range 0.8-1.8 nm, with octahedral shape. According to the reported stability diagram, the rto 38 atoms nanoparticles with different alloy types from rich gold to rich copper composition have been shown to be the most stable structures. In the following work we selected five rto 38 atoms nanoclusters representing Cu_(x-1)Au_(x) of

composition ranging from $x = 0.15$ to $x = 0.36$ and representing three alloy types (regular alloy (RA), core-shell (CS), and skin-heart (SH) structures). As illustrated by Figure 2, the core-shell structure (CS_Cu₃₂Au₆) is formed by six Au atoms in the core and 32 Cu in the shell. The two skin-heart structures at $x=0.21$ and $x=0.36$, are formed by assembling alloyed cores or outer-shells with pure outer-shell (skins) or cores (hearts), respectively. Concerning RA_Cu₃₀Au₈ and SH_Cu₃₀Au₈, at $x=0.21$, the difference between the two structures is that the surface Au atoms are located at the center of the facets and at the edges, respectively. The RA_Cu₂₈Au₁₀ is similar to the RA_Cu₃₀Au₈ but with a richer Au core.

Insert Figure 2

In table 2 the energetic and geometric properties of the free pure Au and Cu and alloyed CuAu nanoclusters are presented. From this table one can see that CS_Cu₃₂Au₆ ($x=0.15$) and SH_Cu₂₄Au₁₄ ($x=0.36$) structures, where Au atoms are mainly on the core, present positive values of excess energy E_{exc} (see Figure 3) and form the largest volume nanoparticles. Considering the Core-Shell structure CSAu₆Cu₃₂ alloy nanoparticles and compared to the monometallic Cu₃₈, the substitution of 6 Cu atoms by Au, stretches the nanoparticles volume by about 8%. For skin heart $x=36$, which is composed of a pure core of 6 Au and an alloyed outer-shell of 8 Au and 24 Cu, the Bi NP shows a volume expansion of 11% compared to pure Cu and a volume decrease of about 14% compared to pure Au.

Structures including a maximum of Au atoms in the outer-shell (RA_Cu₃₀Au₈, SH_Cu₃₀Au₈ ($x=0.21$) and RA_Cu₂₈Au₁₀ with ($x=0.26$)) have negative excess energy values and concomitantly the lowest surface energies. This superior stability could be attributed to the preferential segregation of gold to the surface (cf. Table 1) [75-76]. These results indicate that mixing is favorable for small compositions on gold, as it was expected in view of the bulk alloy.

Insert Table 1

Insert Figure 3

For the composition $x=0.21$, geometry optimizations show that the regular alloyed structure obtained from the regular AuCu₃ bulk, presents an optimal volume only 3% larger than that of pure Cu. The second regular alloyed nanocluster of a composition $x=0.26$ was obtained by substituting 10 Cu atoms by Au; two atoms from the core and 8 from the outer-shell. The volume variation of this structure shows an expansion of 6% compared to the monometallic Cu₃₈. Finally, the skin-heart structure presents similar characteristics as regular alloy structures but according to its low excess energy value this structure is predicted as the most favorable CuAu nanoparticle alloy type. This may be due to the occupation of Au of lower coordinated surface sites (edge sites).

III.3. Deposited nanoparticles

In the following section the effect of the interaction with the titanium oxide supports on the structure, shape and stability of the nanoclusters is analyzed. For clarity, besides Cu and Au monometallics, we focused our analysis of BiM systems on three selected NPs: CS_Cu₃₂Au₆, ($x=0.15$), SH_Cu₃₀Au₈ ($x=0.21$), RA_Cu₃₀Au₈, skin heart ($x=0.21$) structure. Our motivation was to probe the support effect on several nanoclusters with a significant stability difference (strong support effects may stabilize metastable gas phase structures). All computed thermodynamic and geometric data for deposited monometallic and BiM nanoclusters are exposed in tables 2-4 for rutile TiO₂(110) support and in tables 5-7 for anatase TiO₂ (100) support.

Insert Tables from 2 to 7

III.3.1. Au, Cu and CuAu BiM NPs on rutile TiO₂(110)

Insert Figure 4

In Figures 4a and b, the deposited structures of rto(38) Au and Cu nanoparticles over rutile $\text{TiO}_2(110)$ are depicted (see the SI for complementary views). Figures 4c and 4d represent the deposited NPs on anatase support and will be discussed in the next section. Geometry optimizations show that the structure of rto(38) before and after deposition on rutile has not changed much; no strong deformation of the monometallic nanoparticles has occurred. In Tables 2 and 3, the deposition energy and normalized deposition energy of rto(38) are addressed for both Au₃₈ and Cu₃₈ (-201 and -28 $\text{kJ}\cdot\text{mol}^{-1}$ per bond, whereas -493 and -70 $\text{kJ}\cdot\text{mol}^{-1}$ per bond, respectively). The interaction between these nanoparticles and the support forms 7 bonds (see table 4). As shown in Table 2, the deformation energy of rto(38) Au is roughly twice weaker than that of Cu₃₈ (14 versus 34 $\text{kJ}\cdot\text{mol}^{-1}$). The trend obtained for the rutile support is concomitant with a twice larger deformation energy for the deposition of rto(38) Cu with respect to Au. In general, the rutile surface deformation is one order of magnitude larger than that of the metallic nanoclusters. The gain in deposition energy observed for Cu nanocluster is governed by the binding energy (-829 versus -360 $\text{kJ}\cdot\text{mol}^{-1}$) between the NP and the rutile support (largest contribution in the energy decomposition analysis (EDA) model, as illustrated in Table 2). Finally, as depicted in Table 4, the computed geometric deformation ratios of -0.25% and $+0.81\%$, show the negligible contraction of Au nanocluster and the stronger expansion of Cu cluster induced by the contact with the rutile support, respectively.

Regarding the CuAu nanoclusters, the optimal adsorption structures on rutile $\text{TiO}_2(110)$ are depicted in Figures 5a, 5b and 5c (see also the SI for complementary views). The energetic order stability obtained from the calculated E_{exc} in the gas phase ($\text{CS_Cu}_{32}\text{Au}_6 < \text{RA_Cu}_{30}\text{Au}_8 < \text{SH_Cu}_{30}\text{Au}_8$) is strictly opposite to the stability trend on the rutile support

(CS_Cu₃₂Au₆ > RA_Cu₃₀Au₈ > SH_Cu₃₀Au₈). This latter is reflected by the deposition energies of Table 2 in absolute values (698 > 473 > 440 kJ.mol⁻¹). This is also consistent with the relative stability in the gas phase of the two nanoclusters with the same composition RA_Cu₃₀Au₈ and SH_Cu₃₀Au₈ (the less stable is the cluster in gas phase, the larger is its propensity to bind to the support). This analysis is explained by two major contributions of the EDA, i.e. the binding energy between the particle and the support in absolute values (913 > 741 > 705 kJ.mol⁻¹), and the deformation energy of the support, at a lesser extent (168 < 200 < 223). In average, the deformation energy of the supported Au, Cu and CuAu nanoclusters is 41 kJ.mol⁻¹ (cf. Table 2). This is a rather weak deformation which is illustrated by the analysis of the geometric deformation ratios of these clusters by comparing adsorbed structures with gas phase ones (0.8 % in average in Table 4).

Insert Figure 5

III.3.2. Au, Cu and AuCu BiM NPs on anatase TiO₂(100)

The optimal structures of rto(38) Au and Cu on anatase TiO₂(100) have been reported on Figures 4c and 4d (see also the SI for complementary views), while the deposition energies and EDA are addressed in Table 5. For deposited monometallic nanoclusters, our calculations show that both Au and Cu clusters stabilize at the site of the step where the hexagonal face of NP directly interacts with the surface. In such configuration seven atoms of the hexagonal face are bound with seven surface oxygen atoms, five of which belong to the step (O_{2c}) (see Figures 4c and 4d).

The normalized energies per metal-support bond and structural complementary analyses are given in Tables 6-7. Similar to rutile support, rto(38) Au adsorbed on anatase is less strongly bound (-164 kJ.mol⁻¹) than rto(38) Cu (-408 kJ.mol⁻¹). This is mainly explained by the loss of interaction energy (from -600 to -269 kJ.mol⁻¹). Regarding the analysis of deformation

energies (weaker contributions), the trends between Au and Cu nanoclusters are also compatible with those previously predicted for rutile.

For the deposit of CuAu on anatase support, the relaxed adsorption structures are shown in Figures 5 d, 5e and 5f (see also the SI for complementary views). Except for RA_Cu₃₀Au₈, all AuCu nanoclusters stabilize preferentially on the site of the step of the support via the hexagonal face of the NP. CS_Cu₃₂Au₆ nanocluster interacts with the support by connecting seven copper atoms with seven surface oxygens, five of which belong to the step whereas two of which to the terrace. The optimized structure of SH_Cu₃₀Au₈ shows five Cu-O and two Au-O bonds where five bounding surface oxygens are from the step site. Finally, the RA_Cu₃₀Au₈ regular alloy nanocluster with $x = 0.21$ stabilizes preferentially at the terrace site and undergoes a strong deformation (see Figure 5e).

Regarding the relative stability of the three considered clusters on this support with respect to the gas phase, the trend is identical to the one previously exposed for rutile. The least stable cluster in the gas phase (CS_Cu₃₂Au₆) is the most stable one on anatase (-512 kJ.mol^{-1} in Table 5). Once more, this trend is mainly ruled by the binding energy as shown in Table 5 (from -672 to -461 kJ.mol^{-1}). Regarding the average deformation energy of Au, Cu and CuAu nanoclusters (cf. Table 5), the obtained value is weak (44 kJ.mol^{-1}) as the one previously calculated for rutile. The slight increase of energetic cost in average for the adsorbed clusters on anatase is consistent with the small increase of geometric deformation (1.2 % in average according to Table 7).

IV. Discussion

Once the analyses of the monometallic and bimetallic clusters have been examined for each support, the natural next step is the detailed comparison between energetic and structural properties of all these nanoclusters on rutile TiO₂(110) and anatase TiO₂(100). This important

discussion related to the support effect is rarely evoked in the literature of DFT studies for such supported clusters at the nanoscale. In the following, we propose a systematic comparative analysis of the support effect on Au, Cu and various CuAu nanoclusters on the two TiO₂ surfaces. In addition, we also examine and compare the atomic charge distributions from the Bader analysis of all considered deposited systems. All computed Bader charges are provided in the Supporting Information, Figure S1).

The comparative analysis of total deposition energies of all the considered rto(38) mono and bimetallic systems is addressed in Figure 6 for rutile and anatase surfaces. The first key remark is the systematic larger deposition energy predicted on rutile with respect to anatase. Interestingly, this difference of support effect is maximum for the CuAu core-shell bimetallic cluster (-698 kJ.mol^{-1} on rutile versus -512 kJ.mol^{-1} on anatase), for which the gain is 186 kJ.mol^{-1} . According to the EDA, such a difference in favor of rutile is mainly explained by the gain in binding energy (-913 kJ.mol^{-1} for rutile versus -672 kJ.mol^{-1} for anatase) corresponding to 241 kJ.mol^{-1} . The small loss between the variation of binding energy with respect to the one of deposition energy comes from the secondary contribution in the EDA, *i.e.* the deformation energy of the support (168 kJ.mol^{-1} for rutile versus 124 kJ.mol^{-1} for anatase). In this global energetic balance, the main gain resulting from the interaction energy (nanoparticle-support bonding) is thus in part compensated by the larger cost to distort rutile support with respect to anatase. This exceptional effect observed for the supported core-shell clusters can also be understood by looking at the relaxed adsorbed geometries (cf. Figure 5a and 5d). On both rutile and anatase supports, the Au₆ core tends to extract itself from the Cu₃₂ outer-shell, as much as possible (any deformation inducing an energy cost).

Insert Figure 6

A second remark is related to the change of deposition energy which roughly evolves monotonously with the chemical composition (exception of the two core-shell supported

systems); the nanocluster being less stable when the gold content increases. In addition, the deposition energy of regular alloy and skin-heart bimetallic clusters is intermediate between pure and supported Au and Cu nanoclusters.

Coming back to the binding energy between the cluster and the support which is mainly responsible for the stability trends, a first element of comparison is the number of metal-oxygen bonds calculated in the optimal adsorbed structures (the threshold for a bond being 3 Å). In Tables 3, 4 for rutile and 6, 7 for anatase, these total numbers of bonds and associated normalized interaction energies are reported, respectively. The results show that the number is relatively similar for adsorbed clusters on rutile and anatase (an average of 7 bonds), except for the core-shell deposited clusters (11 bonds on anatase versus 6 bonds on rutile). For the monometallic adsorbed clusters, the loss of binding energy between rutile and anatase is identical (26%), the number of bonds being the same. Interestingly, the Bader analysis also shows similar losses of charges for Cu (1.03 e) and Au (0.99 e) clusters between rutile and anatase. The total charge of Cu cluster being -1.595 e on anatase vs. -2.625 e on rutile; and the total charge of Au cluster being 0.57 e on anatase vs. 1.56 e on rutile.

For the bimetallic adsorbed particles, the loss of interaction energy is either similar to the pure clusters (21% for regular alloy from rutile to anatase) or twice stronger for core-shell (a loss of 60%) and skin-heart (a loss of 53%) nanoclusters. For the latter two bimetallic systems, the loss of interaction energy per bond is similar from rutile to anatase, however the origins are alternate: for core-shell the total number of bonds is twice larger as explained before, whereas for skin-heart, the number of bonds varies less. The detailed analyses of Bader charge distributions on the bimetallic systems point out a noticeable effect of the support. For instance, for core-shell structure, formed by negatively charged pure Au core (positively charged Cu shell), a charge loss of 0.24 e in the Au core and a charge gain of 0.57 e in the Cu shell are registered between anatase and rutile. Concerning the supports, the computed total

charges of anatase / rutile in the cases CS_Cu₃₂Au₆ (−1.492 e / −2.298 e) > RA_Cu₃₀Au₈ (−1.457 e / −2.206 e) > SH_Cu₃₀Au₈ (−1.252 e / −1.805 e), follow the trend of deposition energy and confirm the stronger interactions of clusters with rutile support.

A last remark concerns the analysis of the deformation energy of the support which is almost the most important element to analyze for understanding the titania support effect. According to the EDA in Table 2 and 5, the average energy cost to distort rutile upon the cluster deposition is 1.9 larger on rutile than on anatase. This corresponds to a significant average deformation energy of 93 kJ.mol^{−1} for rutile and a stronger charge transfer from clusters adsorbed on rutile support than on anatase. This counterintuitive result illustrates the effective lower propensity of anatase to adapt to the adsorption structure of the metallic cluster with respect to that of rutile, although anatase TiO₂(100) exhibits a higher surface energy than rutile TiO₂(110). This phenomenon is in part compensated by the higher ability of the metallic clusters to deform itself and optimize the binding with the support. As a matter of fact, the average deformation cost for the clusters on anatase is slightly larger than that on rutile (opposite trend with respect to the support) and this compensates the 93 kJ.mol^{−1} at the height of 13% (12 kJ.mol^{−1}).

By the light of this latter analysis, one can expect that the support effect might increase with the size of the deposited metal. In fact, the larger the metallic cluster, the smaller its ability to deform (larger facets being progressively as stable as flat terraces) and to compensate the larger deformation energy registered for anatase.

V. Conclusion

In this paper, we presented and discussed the results of DFT calculations on CuAu nanoclusters deposited on both rutile TiO₂ (110) and anatase TiO₂ (100) supports. The objective was to explore the support effect on the adsorption properties. Regular truncated

octahedron (rto) 38 atoms nanoclusters $\text{Cu}(x-1)\text{Au}(x)$, with x in the range [0.15-0.36], representing three alloy types (regular alloy (RA), core-shell (CS), and skin-heart (SH) structures) were fully optimized in interaction with the support. This selection of AuCu bimetallic nanoparticles has allowed the exploration of various chemical ordering in the core of the cluster but also in the outer-shell, especially for modifying the chemical composition of the facet in contact with the support. A comparative analysis of energetics and structural properties has shown that the adsorption strength of these clusters is systematically larger on rutile than on anatase chosen termination (the most stable cluster being the core-shell $\text{Au}_{32}\text{Cu}_6$). On the basis of an energy decomposition analysis, this gain of stability is essentially due to the enhancement of the binding energy between the nanoparticle and the rutile support, although this is in part counterbalanced by the deformation cost of the oxide which is larger for rutile than for anatase. This result is supported by the Bader analysis of charge transfers between the supports and the metallic nanoclusters. When the gold increases, the stability of the AuCu bimetallic nanoparticles tends to decrease. The larger propensity of bimetallic nanoclusters to distort themselves, aiming to promote the formation of chemical bonds with the support, has been illustrated by examining the deformation energy of the supported clusters. This ability is expected to decrease with the size of the metallic cluster since larger facets than those of rto(38) should be more stable and thus less able to adapt to the geometry of the support. Hence this work illustrates the efficiency of theoretical studies for unraveling the question of the chemical bonding at the complex interface, at the atomic scale between a metal and an oxide surface. It paves the way to advanced DFT studies where larger pure and bimetallic nanoparticles (of several nanometers) will be modeled in interaction with reducible supports, especially with the presence of defects such as oxygen vacancies (another type of support effect).

Acknowledgements

This work was granted access to the HPC resources of [CCRT/CINES/IDRIS] under the allocation 2018 [x2018087369] made by GENCI (Grand Equipement National de Calcul Intensif). A.D acknowledges funding from the Research Center, Scientific Research Deanship, IAU, KSA, under Award No. 2015208.

Supporting Information

See supporting information for the following results:

- i) DFT+U optimizations of TiO₂ bulk materials
- ii) Computed Bader charges of all deposited Au, Cu and CuAu nanoclusters
- iii) Side views of optimized structures of deposited monometallic and bimetallic Au and Cu nanoclusters on rutile (110) and anatase (100) TiO₂ supports.

References

1. Sankar, M.; Dimitratos, N.; Miedziak, P. J.; Wells, P. P.; Kiely, C. J.; Hutchings, G. J. Designing bimetallic catalysts for a green and sustainable future. *Chem. Soc. Rev.* 2012, 41, 8099–8139.
2. Gu, J.; Zhang, Y.-W.; Tao, F. Shape control of bimetallic nanocatalysts through well-designed colloidal chemistry approaches. *Chem. Soc. Rev.* 2012, 41, 8050–8065.
3. Wu, J.; Li, P.; Pan, Y.-T.; Warren, S.; Yin, X.; Yang, H. Surface lattice-engineered bimetallic nanoparticles and their catalytic properties. *Chem. Soc. Rev.* 2012, 41, 8066–8074.
4. Kim, N.R.; Shin, K.; Jung, I.; Shim, M.; Lee, M. Ag-Cu bimetallic nanoparticles with enhanced resistance to oxidation: A combined experimental and theoretical study. *J. Phys. Chem. C.* 2014, 118, 26324–26331.
5. Kitchin, J.R.; Nørskov, J.K.; Barteau, M.A.; Chen, J.G. Role of strain and ligand effects in the modification of the electronic and chemical properties of bimetallic surfaces. *Phys. Rev. Lett.* 2004, 15, 156801-156804
6. Oguz, I.C.; Minéva, T.; Guesmi, H. The effect of Pd ensemble Structure on the O₂ dissociation and CO oxidation mechanisms on Au-Pd(100) surface alloys. *J. Chem. Phys.* 2018, 148, 024701–024710.
7. Louis, C. Chemical Preparation of Supported Bimetallic Catalysts. Gold-based bimetallic, a case study. *Catalysts.* 2016, 6, 110–137.
8. Edwards, J.K.; Solsona, B.E.; Landon, P.; Carley, A.F.; Herzing, A.; Kiely, C.J.; Hutchings, G.J. Direct synthesis of hydrogen peroxide from H and O using TiO₂-supported Au-Pd catalysts. *J. Catal.* 2005, 236, 69–79.
9. Zhu, B.; Thrimurthu, G.; Delannoy, L.; Louis, C.; Mottet, C.; Creuze, J.; Legrand, B.; Guesmi, H. Evidence of Pd segregation and stabilization at edges of AuPd nano-clusters in the presence of CO: a combined DFT and DRIFTS study. *J. Catal.* 2013, 308, 272-281.
10. Chimentao, R.J.; Medina, F.; Fierro, J.L.G.; Llorca, J.; Sueiras, J.E.; Cesteros, Y.; Salagre, P. Propene epoxidation by nitrous oxide over Au-Cu/TiO₂ alloy catalysts. *J. Mol. Catal. A* 2007, 274, 159–168.
11. Delannoy, L.; Thrimurthulu, G.; Reddy, P.S.; Méthivier, C.; Nelayah, J.; Reddy, B.M.; Ricolleau, C.; Louis, C. Selective hydrogenation of butadiene over TiO₂ supported copper, gold and gold-copper catalysts prepared by deposition precipitation. *Phys. Chem. Chem. Phys.* 2014, 16, 26514–26527.

12. Pauwels, B.; van Tendeloo, G.; Zhurkin, E.; Hou, M.; Verschoren, G.; Kuhn, L.T.; Bouwen, W.; Lievens, P. Transmission electron microscopy and Monte Carlo simulations of ordering in Au-Cu clusters produced in a laser vaporization source. *Phys. Rev. B.* 2001, 63, 165406–165415.
13. Sandoval, A.; Aguilar, A.; Louis, C.; Traverse, A.; Zanella, R. Bimetallic Au-Ag/TiO catalyst prepared by 2 deposition-precipitation. High activity and stability in CO oxidation. *J. Catal.* 2011, 281, 40–49.
14. Menezes, W.G.; Zielasek, V.; Thiel, K.; Hartwig, A.; Bäumer, M. Effects of particle size, composition, and support on catalytic activity of AuAg nanoparticles prepared in reverse block copolymer micelles as nanoreactors. *J. Catal.* 2013, 299, 222–231.
15. Gallo, A.; Montini, T.; Marelli, M.; Minguzzi, A.; Gombac, V.; Psaro, R.; Fornasiero, P.; Santo, V.D. H₂ production by renewables photoreforming on Pt-Au/TiO catalysts activated by reduction. *ChemSusChem* 2012, 5, 1800–1811.
16. Na, H.; Zhu, T.; Liu, Z. Effect of preparation method on the performance of Pt-Au/TiO₂ catalysts for the catalytic co-oxidation of HCHO and CO. *Catal. Sci. Technol.* 2014, 4, 2051–2057.
17. Juarez, MF; Soldano, G; Guesmi, H; Tielens, F; Santos, E. Catalytic properties of Au electrodes modified by an underlayer of Pd . *Surf. Sci.* 2015, 631, 235–247.
18. Su, R.; Tiruvalam, R.; Logsdail, A. J.; He, Q.; Downing, C. A.; Jensen, M. T.; Dimitratos, N.; Kesavan, L.; Wells, P. P.; Bechstein, R. et al. Designer titania-supported AuPd nanoparticles for efficient photocatalytic hydrogen production. *ACS Nano.* 2014, 8, 3490–3497.
19. Hai, Z.; El Kolli, N.; Bahena Uribe, D.; Beaunier, P.; José-Yacamán, M.; Vigneron, J.; Etcheberry, A.; Sorgues, S.; Colbeau-Justin, C.; Chen, J. et al. Modification of TiO₂ by bimetallic Au–Cu nanoparticles for wastewater treatment. *J. Mater. Chem. A* 2013, 1, 10829.
20. Nahar, S.; Zain, M. F. M. ; Kadhum, A. A. H.; Hasan, H. A.; Hasan Md. R. H. Advances in Photocatalytic CO₂ Reduction with Water: A Review. *Materials* 2017,10, 629.
21. Hai, Z.; El Kolli, N.; Chen, J.; Remita, H. Radiolytic synthesis of Au–Cu bimetallic nanoparticles supported on TiO₂: application in photocatalysis. *New J. Chem.* 2014, 38, 5279.
22. Diebold, U. The surface science of titanium dioxide. *Surf. Sci. Rep.* 2003, 48, 53–229.
23. Tauster, S.J.; Fung, S. C.; Baker, R.T.K.; Horsley, J.A. Strong interactions in supported-metal catalysts. *Science* 1981, 211, 1121–1125.

24. Kominami H.; Kalo J.-I.; Takada Y.; Doushi Y.; Ohtani B.; Nishimoto S.-I.; Inoue M.; Inui T.; Kera Y. Novel synthesis of microcrystalline titanium(IV) oxide having high thermal stability and ultra-high photocatalytic activity: thermal decomposition of titanium(IV) alkoxide in organic solvents. *Catal. Lett.* 1997, 46, 235–240.
25. Neațu, Ș.; Maciá-Agulló, J.A.; Concepción, P.; Garcia, H. Gold–Copper Nanoalloys supported on TiO₂ as photocatalysts for CO₂ reduction by water. *J. Am. Chem. Soc.* 2014, 136, 15969–15976.
26. Panayotov, D. A.; Morris, J. R. Surface chemistry of Au/TiO₂: Thermally and photolytically activated reactions. *Surf. Sci. Rep.* 2016, 71, 77–271.
27. Subramanian, V.; Wolf, E. E.; Kamat, P. V. Catalysis with TiO₂/Gold nanocomposites: effect of metal particle size on the Fermi Level equilibration. *J. Am. Chem. Soc.* 2004, 126, 4943–4950.
28. Li, H.; Bian, Z.; Zhu, J.; Huo, Y.; Li, H.; Lu, Y. Mesoporous Au/TiO₂ nanocomposites with enhanced photocatalytic activity. *J. Am. Chem. Soc.* 2007, 129, 4538–4539.
29. Murdoch, M.; Waterhouse, G. I. N.; Nadeem, M. A.; Metson, J. B.; Keane, M. A.; Howe, R. F.; Llorca, J.; Idriss, H. The effect of gold loading and particle size on photocatalytic hydrogen production from ethanol over Au/TiO₂ nanoparticles. *Nat. Chem.* 2011, 3, 489–492.
- [30] Liu, X. Y.; Wang, A.; Zhang, T.; Mou, C.-Y. Catalysis by gold: New insights into the support effect. *Nano Today* 2013, 8, 403–416.
- 31 Delannoy, L.; Weiher, N.; Tsapatsaris, N.; Beesley, A.M.; Nchari, L.; Schroeder, S.L.M.; Louis, C. Reducibility of supported gold (III) precursors: influence of the metal oxide support and consequences for CO oxidation activity. *Top. Catal.* 2007, 44, 263–273.
32. Chen, M.; Cai, Y.; Yan, Z.; Goodman, D.W. On the origin of the unique properties of supported Au nanoparticles. *JACS.* 2006, 128, 6341– 6346.
33. Chen, M.; Goodman, D.W. Catalytically active gold on ordered titania supports. *Chem. Soc. Rev* 2008, 37, 1860–1870.
34. Li, L.; Gao Y.; Li, H.; Zhao, Y.; Pei, Y.; Chen, Z.; Zeng, X. C. CO oxidation on TiO₂ (110) supported subnanometer gold clusters: Size and shape effects. *JACS.* 2013, 135, 19336–19346.
35. Turner, M.; Golovko, V.B.; Vaughan, O.P.H.; Abdulkin, P.; Berenguer-Murcia, A.; Tikhov, M.S.; Johnson, B.F.G.; Lambert, R.M. Selective oxidation with dioxygen by gold nanoparticle catalysts derived from 55-atom clusters. *Nature* 2008, 454, 981–984.

36. Pillay, D.; Hwang, G. S. Growth and structure of small gold particles on rutile TiO₂ (110). *Phys. Rev. B* 2005, 72, 205422–205428.
37. Pillay, D.; Hwang, G. S. Structure of small Au_n, Ag_n, and Cu_n clusters (n ≤ 20) on rutile TiO₂(110): A density functional theory study. *Journal of Molecular Structure: J. Mol. Struct. THEOCHEM*, 2006, 771, 129–133.
38. Jiang, Z. Y.; Zhao, Z.-Y. Density functional theory study on the metal–support interaction between a Au₉ cluster and an anatase TiO₂(001) surface. *Phys. Chem. Chem. Phys.*, 2017, 19, 22069–22077.
39. Puigdollers, A. R.; Schlexer, P.; Pacchioni G. Gold and silver clusters on TiO₂ and ZrO₂ (101) surfaces: role of dispersion forces. *J. Phys. Chem. C* 2015, 119, 15381–15389.
40. Vilhelmsen, L. B.; Hammer, B. Identification of the catalytic site at the interface perimeter of Au clusters on rutile TiO₂(110). *ACS Catal.* 2014, 4, 1626–1631.
41. Vilhelmsen, L. B.; Hammer, B. A genetic algorithm for first principles global structure optimization of supported nano structures. *J. Chem. Phys.* 2014, 141, 044711–044722.
42. Ding, R.-L.; Jia, J.; Wu H.-S. The growth pattern of Au_n (n = 1–20) clusters absorbed on rutile TiO₂ (1 1 0) surfaces. *Applied Surface Science* 2015, 359, 729–735.
43. Barcaro, G.; Fortunelli, A.; Rossi, G.; Nita, F.; R. Ferrando. Electronic and structural shell closure in AgCu and AuCu nanoclusters. *J. Phys. Chem. B* 2006, 110, 23197–23203.
44. Darby, S.; Mortimer-Jones, T. V.; Johnston, R. L.; Roberts, C. Theoretical study of Cu–Au nanoalloy clusters using a genetic algorithm. *J. Chem. Phys.* 2002, 116, 1536–1550.
45. Ferrando, R.; Fortunelli, A.; Rossi, G. Quantum effects on the structure of pure and binary metallic nanoclusters. *Phys. Rev. B* 2005, 72, 085449–085458.
46. Rapallo, A.; Rossi, G.; Ferrando, R.; Fortunelli, A.; Curley, B. C.; Lloyd, L. D.; Tarbuck, G. M.; Johnston, R. L. Global optimization of bimetallic cluster structures. I. Size-mismatched Ag–Cu, Ag–Ni, and Au–Cu systems. *J. Chem. Phys.* 2005, 122, 194308–194331.
47. Hsu, P. J.; Lai, S. K. Structures of bimetallic clusters. *J. Chem. Phys.* 2006, 124, 044711–044722.
48. Tran, D. T.; Johnston, R. L. Theoretical study of Cu₃₈nAu_n clusters using a combined empirical potential–density functional approach. *Phys. Chem. Chem. Phys.* 2009, 11, 10340–10349.
49. Jiang, Z.-Y.; Zhao, Z.-Y. Adsorption of Au_xCu_y (x + y = 1, 2, 3) nanoclusters on the anatase TiO₂(101) surface and their catalytic activity: a density functional theory study. *Catal. Sci. Technol.* 2017, 7, 5709–5722

50. Jiang, Z.-Y.; Zhao, Z.-Y. Comparison studies of interfacial energetic and electronic properties of bimetallic AuCu/TiO₂ hetero-structures from DFT calculations. *Inorg. Chem. Front.* 2018, 5, 1062–1075.
51. Blochl, P. E.; Jepsen, O.; Andersen, O. K. Improved tetrahedron method for Brillouin-zone integrations. *Phys. Rev. B: Condens. Matter Mater. Phys.* 1994, 49, 16223–16234.
52. Kresse, G.; Joubert, D. From ultrasoft pseudopotentials to the projector augmented-wave method. *Phys. Rev. B: Condens. Matter Mater. Phys.* 1999, 59, 1758–1775.
53. Kresse, G.; Hafner, J. Ab initio molecular dynamics for liquid metal. *Phys. Rev. B: Condens. Matter Mater. Phys.* 1993, 47, 558–561.
54. Perdew, P.; Burke, K.; Ernzerhof, M. Generalized gradient approximation made simple. *Phys. Rev. Lett.* 1996, 77, 3865–3868.
55. Morgan, B. J.; Watson, G.W. A dft+u description of oxygen vacancies at the TiO₂ rutile (110) surface. *Surf. Sci* 2007 601, 5034–5041.
56. Tang, H.; Berger, H.; Schmid, P. E.; Lévy, F. Photoluminescence in TiO₂ anatase single crystals, *Solid State Commun.* 1993, 87, 847–850.
57. Bengone, O.; Alouani, M.; Blöchl, P.; Hugel, J. Implementation of the projector augmented-wave LDA+U method: Application to the electronic structure of NiO. *Phys. Rev. B* 2000, 62, 16392–16401.
58. Altland, A.; Simons, B. *Condensed matter field theory.* Cambridge University Press, Chapter 2, 2010.
59. Surján, P.R. *Second quantized approach to quantum chemistry.* Springer-Verlag, Heidelber, Chapter 10, 1989.
60. Dudarev, S.L.; Botton, G.A.; Savrasov, S.Y.; Humphreys, C.J.; Sutton, A.P. Electronenergy-loss spectra and the structural stability of nickel oxide: An LSDA+U study. *Phys. Rev. B* 1998, 57, 1505–1509.
61. Iachella, M.; Le Bahers, T.; Loffreda, D. Diffusion kinetics of gold and copper atoms on pristine and reduced rutile TiO₂(110) surfaces. *J. Phys. Chem. C* 2018, 122, 3824–3837.
62. Monkhorst, H. J.; Pack, J.D. Special points for brillouin-zone integrations. *Phys. Rev. B* 1976, 13, 5188–5192.
63. Cleveland, C.L.; Landman, U. The energetics and structure of nickel clusters: Size dependence. *J. Chem. Phys.* 1991, 94, 7376–7396.
64. Rapallo, A.; Rossi, G.; Ferrando, R.; Fortunelli, A.; Curley, B. C.; Lloyd, L. D.; Tarbuck, G. M.; Johnston, R. L. Global optimization of bimetallic cluster structures. I. Size-

mismatched Ag–Cu, Ag–Ni, and Au–Cu systems. *J. Chem. Phys.* 2005, 122, 194308–194320.

65. Ferrando, R.; Jellinek, J.; Johnston, R. L. Nanoalloys: From theory to applications of alloys Clusters and nanoparticles. *Chem. Rev.* 2008, 108, 845–910.

66. Iachella, M. PhD Thesis, Ecole Normale Supérieure de Lyon, France, 2016.

67. Hammer, B. Adsorption, diffusion, and dissociation of NO, N and O on flat and stepped Ru(0001). *Surf. Sci* 2000, 459, 323 – 348.

68. Dupont, C.; Jugnet, Y.; Loffreda, D. Theoretical evidence of PtSn alloy efficiency for CO oxidation. *JACS* 2006, 128, 9129–9136.

69. Bader, F.W. *Atoms in molecules: a quantum theory*, Oxford Science, Oxford, UK, 1990.

70. Sanville, E.; Kenny, S.D.; Smith, R.; Henkelman, G. Improved grid-based algorithm for Bader charge allocation. *J. Comput. Chem.* 2007, 28, 899–908.

71. U. Diebold. *The surface science of titanium dioxide*. *Surf. Sci. Rep.* 2003, 48, 53–229.

72. Vinet, P.; Ferrante, J.; Smith, J. R.; Rose, J. H. A universal equation of state for solids. *J. Phys. C: Solid State Phys.* 1986, 19, 467–473.

73. Lazzeri, M.; Vittadini, A.; Selloni, A. Structure and energetics of stoichiometric TiO₂ anatase surfaces. *PRB* 2001, 63, 155409–155417.

74. Ma, X.; Dai, Y.; Guo, M.; Huang, B. Relative photooxidation and photoreduction activities of the {100}, {101}, and {001} surfaces of anatase TiO₂. *Langmuir* 2013, 29, 13647–13701.

75. Dhifallah, M.; Dhouib, A.; Aldulaijan, S.; Drenzo, F.; Guesmi, H. First-principles study of Au-Cu alloy surface changes induced by gas adsorptions CO, NO or O₂. *J. Chem. Phys.* 2016, 145, 024701–024708.

76 Sansa, M.; Dhouib, A.; Guesmi, H. Density functional theory study of CO-inducing segregation in gold-based alloys, *J. Chem. Phys.* 2014, 141, 064709–064715.

Tables

Table 1: Energetic (Energy excess and surface energy) and geometric (average atomic distance and volume) descriptors of isolated pure and BiM NPs (GGA PBE level).

Au content (x)	Free NPs	ΔE_{exc} (eV/atom)	Γ (eV. \AA^{-2})	d(\AA)	V(\AA^3)
0	rto(38)Cu	0.000	0.043	2.48	1694.9
0.157	CS_Cu ₃₂ Au ₆	+0.108	0.045	2.58	1902.6
0.210	RA_Cu ₃₀ Au ₈	-0.037	0.040	2.52	1780.3
0.210	SH_Cu ₃₀ Au ₈	-0.074	0.038	2.53	1788.8
0.263	RA_Cu ₂₈ Au ₁₀	-0.052	0.040	2.56	1854.9
0.368	SH_Cu ₂₄ Au ₁₄	+0.034	0.042	2.62	1986.2
1	rto(38)Au	0.000	0.028	2.83	2499.2

Table 2: Energetics (deposition, deformation and interaction energies) for optimized rto(38)Au, rto(38)Cu, Core-shell CS_Cu₃₂Au₆, regular alloy RA_Cu₃₀Au₈, skin heart SH_Cu₃₀Au₈ nanoparticles adsorbed on the rutile TiO₂ (110) support.

Nanocluster (kJ.mol ⁻¹)	$\Delta E_{deposition}^{NP/TiO_2}$	ΔE_{deform}^{NP}	$\Delta E_{deform}^{TiO_2}$	$\sum \Delta E_{deform}$	$\Delta E_{interaction}^{NP*/TiO_2^*}$
rto(38) Au	-201	14	144	158	-359
rto(38)Cu	-493	34	302	336	-829
CS_Cu ₃₂ Au ₆	-698	47	168	215	-913
RA_Cu ₃₀ Au ₈	-473	68	200	268	-741
SH_Cu ₃₀ Au ₈	-440	43	223	266	-706

Table 3: Energetics (average deposition and interaction energies) for optimized rto(38)Au, rto(38)Cu, Core-shell CS_Cu₃₂Au₆, regular alloy RA_Cu₃₀Au₈, skin heart SH_Cu₃₀Au₈ nanoparticles adsorbed on the rutile stoichiometric TiO₂ (110) support.

Nanocluster (kJ.mol ⁻¹)	$\langle \Delta E_{deposition}^{NP/TiO_2} \rangle$	$\langle \Delta E_{interaction}^{NP*/TiO_2^*} \rangle$
rto(38) Au	-28	-51
rto(38)Cu	-70	-118
CS_Cu ₃₂ Au ₆	-116	-152
RA_Cu ₃₀ Au ₈	-68	-106
SH_Cu ₃₀ Au ₈	-62	-100

Table 4 : Geometric properties (average metal-metal bond lengths of the NP optimized gas phase, of the NP optimized on the support, geometric deformations and the numbers of bounds connecting the NP with the support) for rto(38)Au, rto(38) Cu, Core-shell CS_Cu₃₂Au₆, regular alloy RA_Cu₃₀Au₈, skin heart SH_Cu₃₀Au₈ nanoparticles adsorbed on the rutile stoichiometric TiO₂ (110) support.

Nanocluster	$\overline{d_{M-M}^{NP}}$ (Å)	$\overline{d_{M-M}^{NP^*}}$ (Å)	$\Delta \overline{d_{M-M}}$ (Å)	r_{deform} (%)	$N_b^{NP-TiO_2}$
rto(38) Au	2.827	2.82	-0.01	-0.25	7
rto(38)Cu	2.48	2.50	0.02	0.81	7
CS_Cu ₃₂ Au ₆	2.59	2.54	-0.05	-1.93	6
RA_Cu ₃₀ Au ₈	2.55	2.57	0.02	0.78	7
SH_Cu ₃₀ Au ₈	2.55	2.56	0.01	0.39	7

Table 5: Energetics (deposition, deformation and interaction energies) for optimized *rto(38)Au*, *rto(38)Cu*, Core-shell *CS_Cu₃₂Au₆*, regular alloy *RA_Cu₃₀Au₈*, skin heart *SH_Cu₃₀Au₈* nanoparticles adsorbed on the anatase *TiO₂ (100)* support.

Nanocluster (kJ.mol ⁻¹)	$\Delta E_{deposition}^{NP/TiO_2}$	ΔE_{deform}^{NP}	$\Delta E_{deform}^{TiO_2}$	$\Sigma \Delta E_{deform}$	$\Delta E_{interaction}^{NP*/TiO_2^*}$
<i>rto(38) Au</i>	-164	34	71	105	-269
<i>rto(38)Cu</i>	-408	51	141	192	-600
<i>CS_Cu₃₂Au₆</i>	-512	36	124	160	-672
<i>RA_Cu₃₀Au₈</i>	-389	70	130	200	-589
<i>SH_Cu₃₀Au₈</i>	-323	31	107	138	-461

Table 6: Energetics (average deposition and interaction energies) for optimized *rto(38)Au*, *rto(38)Cu*, Core-shell *CS_Cu₃₂Au₆*, regular alloy *RA_Cu₃₀Au₈*, skin heart *SH_Cu₃₀Au₈* nanoparticles adsorbed on the anatase stoichiometric *TiO₂ (100)* support.

Nanocluster (kJ.mol ⁻¹)	$\langle \Delta E_{deposition}^{NP/TiO_2} \rangle$	$\langle \Delta E_{interaction}^{NP*/TiO_2^*} \rangle$
<i>rto(38) Au</i>	-23	-38
<i>rto(38)Cu</i>	-58	-86
<i>CS_Cu₃₂Au₆</i>	-47	-61
<i>RA_Cu₃₀Au₈</i>	-55	-84
<i>SH_Cu₃₀Au₈</i>	-46	-66

Table 7: Geometric properties (average metal-metal bond lengths of the NP optimized gas phase, of the NP optimized on the support, geometric deformations and the numbers of bounds connecting the NP with the support) for optimized rto(38)Au, rto(38) Cu, Core-shell CS_Cu₃₂Au₆, regular alloy RA_Cu₃₀Au₈, skin heart SH_Cu₃₀Au₈ nanoparticles adsorbed on the anatase stoichiometric TiO₂ (100) support.

Nanocluster	$\overline{d_{M-M}^{NP}}$ (Å)	$\overline{d_{M-M}^{NP*}}$ (Å)	$\Delta\overline{d_{M-M}}$ (Å)	r_{deform} (%)	$N_b^{NP-TiO_2}$
rto(38) Au	2.825	2.835	0.01	0.35	7
rto(38)Cu	2.482	2.516	0.034	1.37	7
CS_Cu ₃₂ Au ₆	2.580	2.640	0.060	2.32	11
RA_Cu ₃₀ Au ₈	2.523	2.594	0.071	2.81	7
SH_Cu ₃₀ Au ₈	2.527	2.570	0.043	1.70	7

Figure captions

Figure 1: Lateral (upper part) and top (downmost part) views of TiO₂ support surfaces (a) TiO₂ (110) rutile, (b) TiO₂ (100) anatase. Red and blue balls are oxygen and titanium atoms, respectively.

Figure 2: Optimal structures of free Cu_(x-1)Au_(x) nanoclusters of composition x in the range [0.15-0.36], of truncated octahedral shape and of total number of atoms of 38. Au (yellow), Cu (orange). **Notation :** CS = Core-Shell, RA = Regular Alloy, SH = Skin heart

Figure 3: DFT calculated excess energies E_{exc} (eq. 2) of free CuAu nanoclusters as a function of Au content (x). See Figure 2 for the definitions.

Figure 4: Optimized structures of deposited monometallic Au and Cu nanoclusters on (a,b) rutile (110) and (c,d) anatase (100) TiO₂ supports. The yellow, brown, blue and red colored balls represent Au, Cu, Ti and O, respectively.

Figure 5: Structures of optimized CuAu nanoparticles deposited on (a,b,c) the rutile TiO₂ (110) and (d,e,f) anatase (100) TiO₂ supports. Ti atoms are represented in blue, O in red, Au in yellow and Cu in brown.

Figure 6: Evolution of the computed energy deposition of Au, Cu and CuAu nanoclusters on anatase TiO₂ (100) (red line) and rutile TiO₂ (110) (blue line), as a function of Au content (x).

Figures

Figure 1

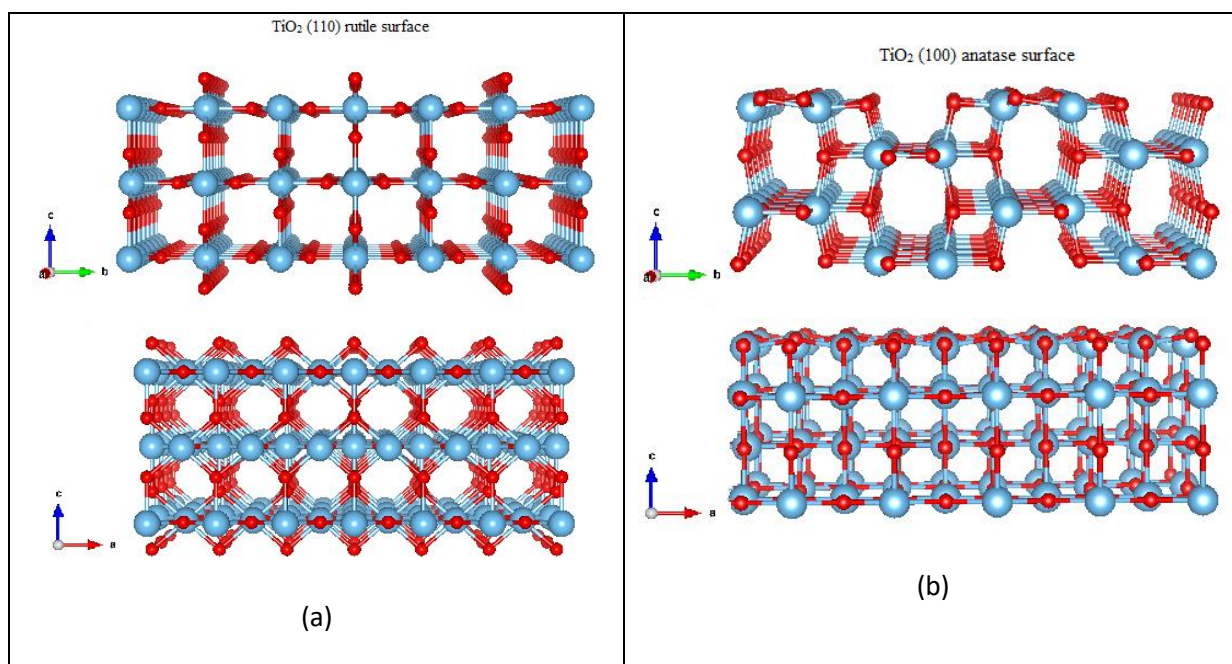


Figure 2

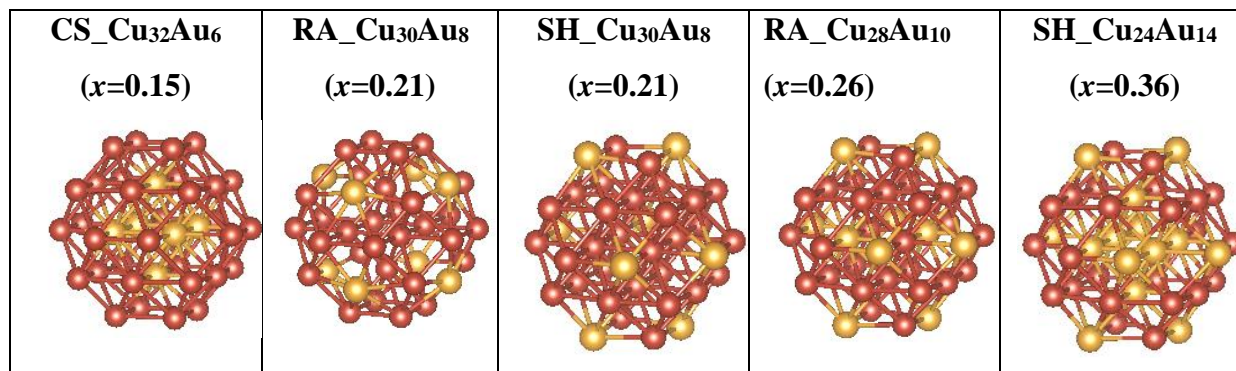


Figure 3

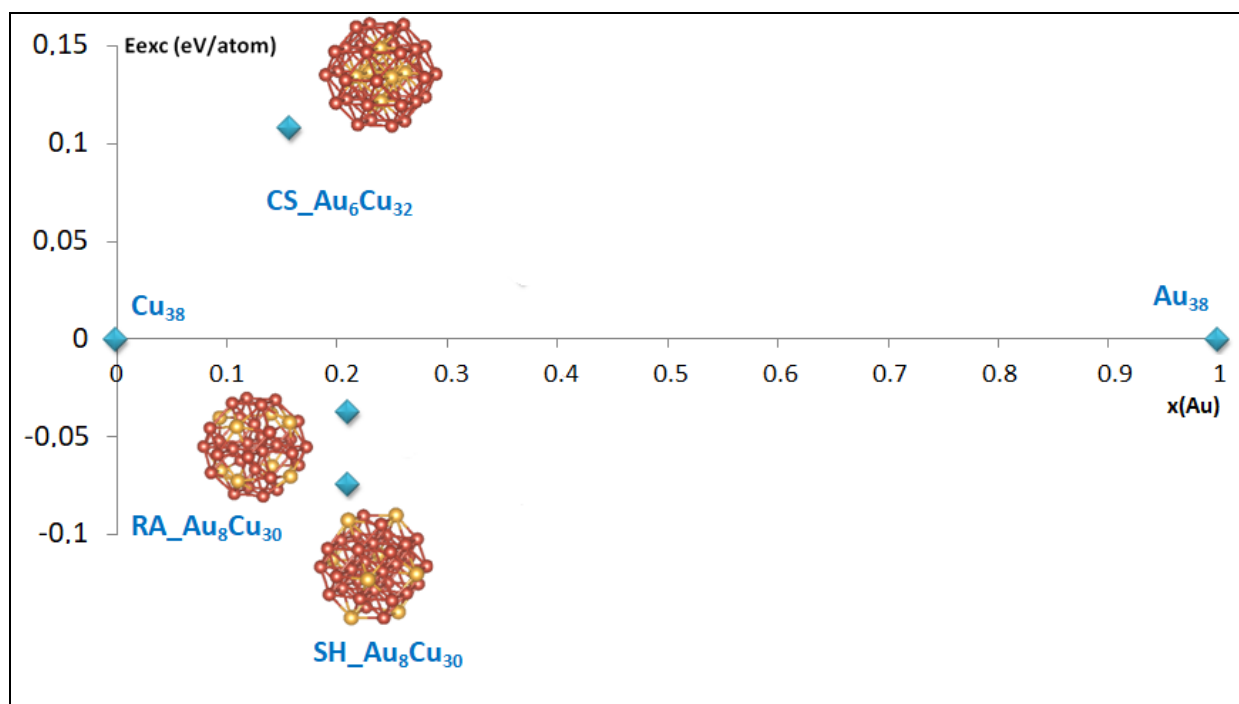
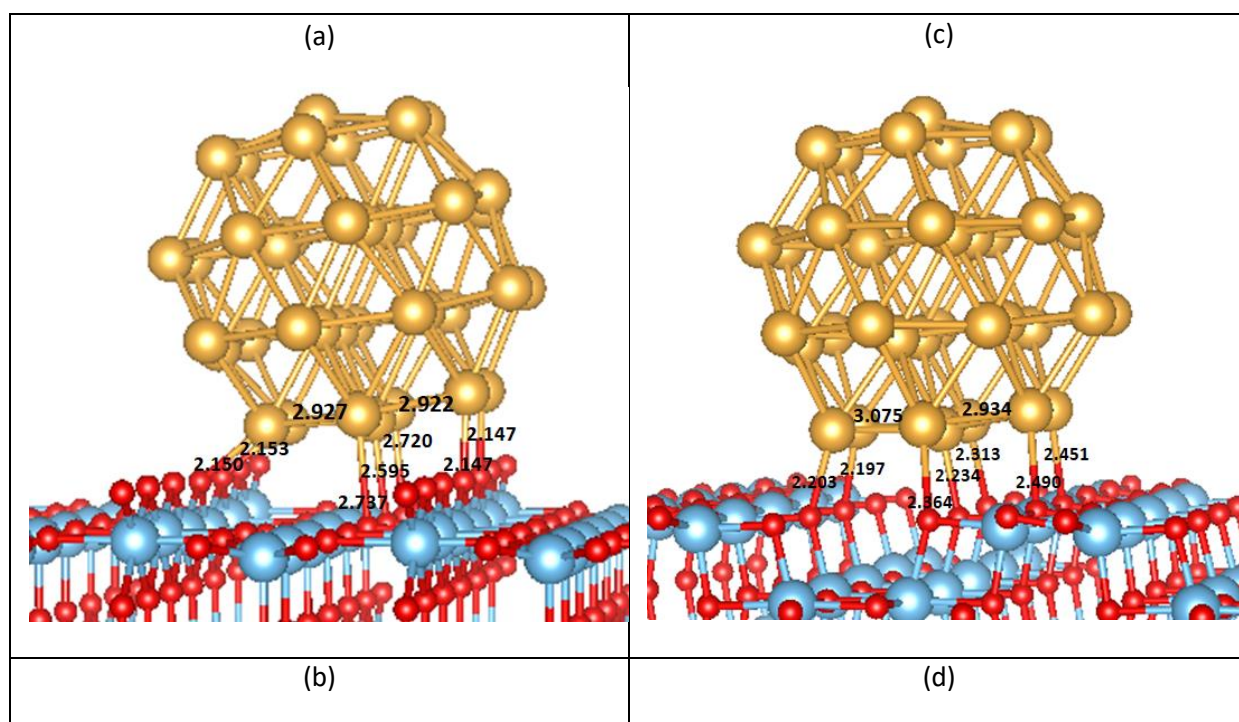


Figure 4



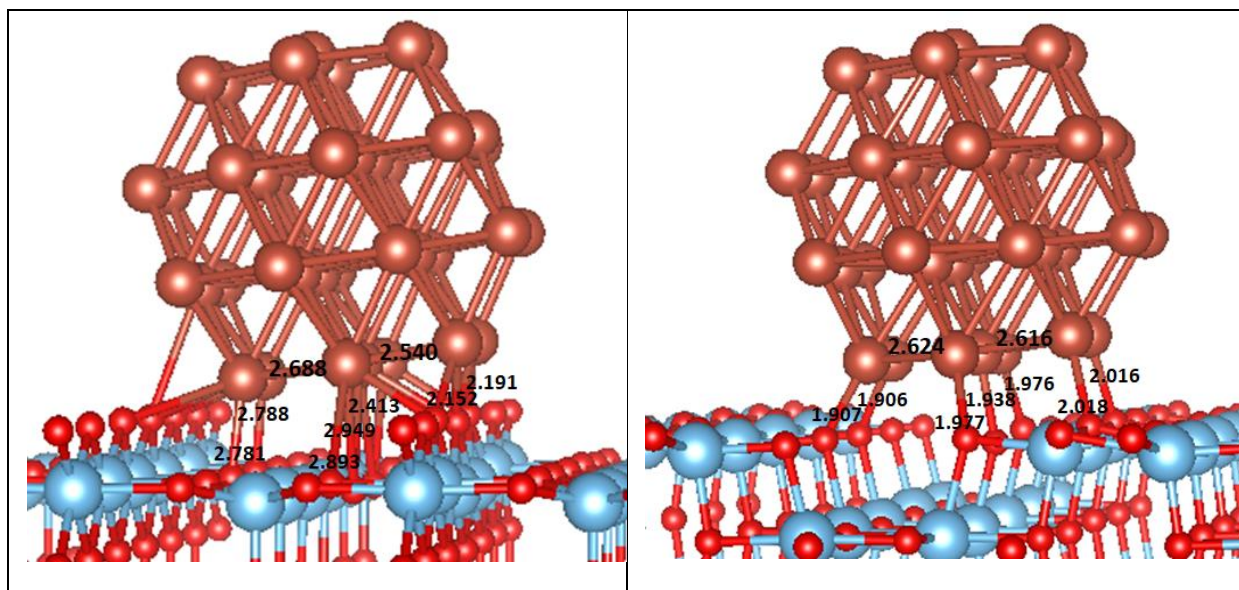
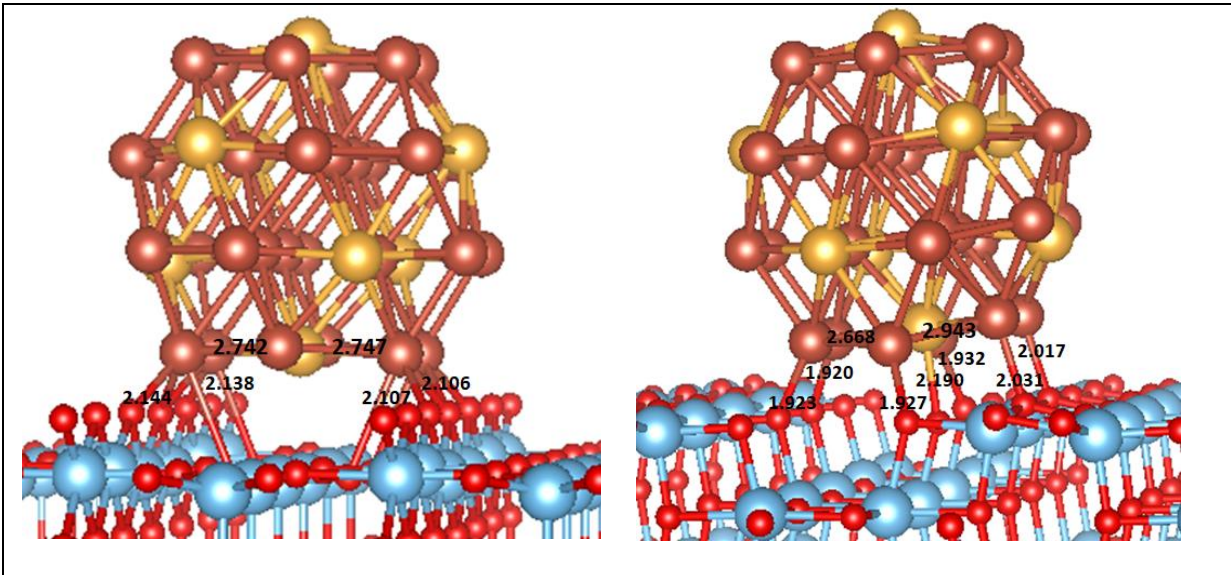


Figure 5

Rutile TiO ₂ (110) support	Anatase TiO ₂ (100) support
CS_Cu ₃₂ Au ₆	
(a)	(d)
RA_Cu ₃₀ Au ₈	
(b)	(e)



SH_Cu₃₀Au₈

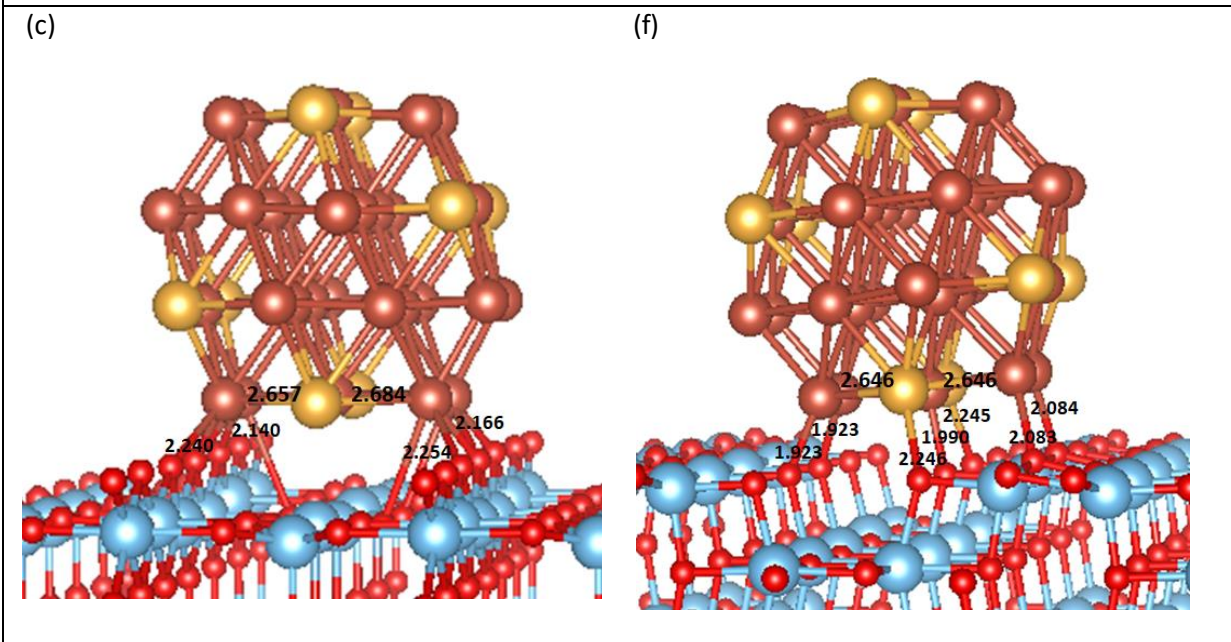
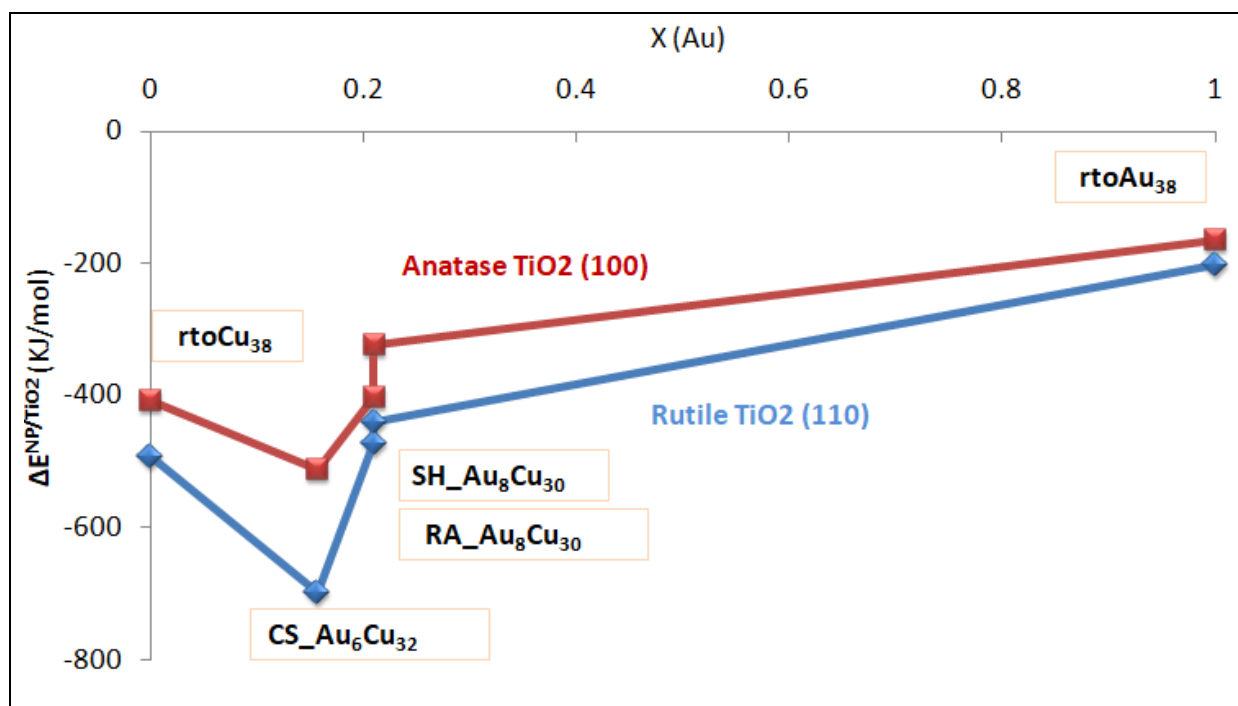


Figure 6



TOC Graphic

